Superconducting proximity effect and possible evidence for Pearl vortices in a candidate topological insulator

Duming Zhang, Jian Wang, Ashley M. DaSilva, Joon Sue Lee, Humberto R. Gutierrez, Moses H. W. Chan,
Jainendra Jain, and Nitin Samarth[*]

*The Center for Nanoscale Science and Department of Physics, The Pennsylvania State University, University Park,
Pennsylvania 16802-6300, USA*

We report the observation of the superconducting proximity effect in nanoribbons of a candidate topological insulator (Bi_2Se_3), which is interfaced with superconducting (tungsten) contacts. We observe a supercurrent and multiple Andreev reflections for channel lengths that are much longer than the inelastic and diffusive thermal lengths deduced from normal-state transport. This suggests that the proximity effect couples preferentially to a ballistic surface transport channel, even in the presence of a coexisting diffusive bulk channel. When a magnetic field is applied perpendicular to the plane of the nanoribbon, we observe magnetoresistance oscillations that are periodic in magnetic field. Quantitative comparison with a model of vortex blockade relates the occurrence of these oscillations to the formation of Pearl vortices in the region of proximity-induced superconductivity.

PACS number(s): 73.25.+i, 03.65.Vf, 71.70.Ej, 72.15.Rn

I. INTRODUCTION

Proximity-induced superconductivity in superconductor-normal (SN) conductor junctions has a long history of theoretical and experimental study.[1] Recently, the superconducting proximity effect has attracted renewed theoretical attention within the context of topological insulators (TIs), materials wherein topologically protected, spin-polarized surface states are created by the combination of strong spin-orbit coupling and time-reversal symmetry.[2,3] Interfacing a TI with a conventional superconductor is of fundamental interest for a variety of reasons. At such interfaces, theory predicts the formation of zero-energy-mode quasiparticles that are condensed matter analogs of elementary fermionic excitations envisioned by Majorana, but not yet observed in nature.[4–6] Furthermore, the "locking" of spin and momentum in TI surface states raises important theoretical questions about the nature of the proximity effect at TI and superconductor junctions,[7] and recent experiments suggest that the measurement geometry could have a significant influence on the observed phenomena.[8] Evidence for the proximity effect was provided in an early study[9] that interfaced a superconductor with $Bi_{1-x}Sb_x$, a material now recognized[10,11] as a three-dimensional (3D) TI. More recently,[12] a supercurrent was observed in thin exfoliated samples of another TI (Bi_2Se_3). Bulk superconductivity has also been seen in compounds derived from a parent TI.[13,14] However, systematic studies of proximity-induced superconductivity in candidate TIs are still in their infancy.

In this paper, we discuss measurements of the proximity effect in mesoscopic Bi_2Se_3 channels interfaced with superconducting tungsten (W) leads. Our principal aim is to report the observation of two experimental results. First, we show that, even in nonideal TI samples with bulk conduction, ballistic transport in the surface states can manifest through the persistence of a supercurrent and multiple Andreev reflections over significantly longer distances than the phase breaking and diffusive thermal lengths deduced from (bulk-dominated) normal-state transport. Second, at temperatures above the onset of complete superconductivity, we observe magnetoresistance (MR) oscillations that can not be understood using conventional scenarios such as fluxoid quantization or the Aharonov-Bohm effect. Instead, the data are *quantitatively* explained using a recent model[15] that relates MR oscillations in superconducting channels to the "Weber blockade" of Pearl vortices. The combined observation of proximity-induced superconductivity and vortices in a TI-superconductor configuration could be relevant in the ongoing search for Majorana fermions.[4–6]

II. SYNTHESIS AND CHARACTERIZATION OF Bi_2Se_3 NANORIBBONS

The Bi_2Se_3 nanoribbons studied here were synthesized via gold catalyzed vapor-liquid-solid mechanism using a horizontal tube furnace.[16,17] The source material Bi_2Se_3 shots (Alfa Aesar, 99.999%) were placed in the center of the hot furnace where the temperature was kept at $\sim 530\,^{\circ}$C during the growth. A Si (100) substrate dispersed with gold catalyst particles (~ 20 nm in diameter) was placed downstream at the cold region zone. The tube was flushed with Ar several times before the growth to remove residual oxygen. A 60-sccm Ar flow was kept at 1 Torr at the base pressure of ~ 10 mTorr during the growth. The furnace was cooled down to room temperature after a 1 hour and 30 minute growth. Figure 1(a) shows a scanning electron microscopy (SEM) image of an as-grown sample. A typical growth usually produces nanoribbons with thickness $60 \lesssim t \lesssim 100$ nm, width $200 \lesssim w \lesssim 500$ nm, and length $2 \lesssim L \lesssim 30\ \mu$m. Figure 1(b) shows a high-resolution transmission electron microscopy (TEM) image from the edge of a typical nanoribbon. The interplanar distance along the nanoribbon growth direction is 0.21 nm, which is consistent with the Bi_2Se_3 lattice constant ($a = b = 0.4140$ nm, $c = 2.8636$ nm). Figure 1(c) is a selected area electron diffraction pattern from the same ribbon: all the nanoribbons we have studied so far show a growth direction along [11$\bar{2}$0]. The clear lattice fringes and the electron diffraction pattern indicate that these ribbons are single crystals with little disorder.
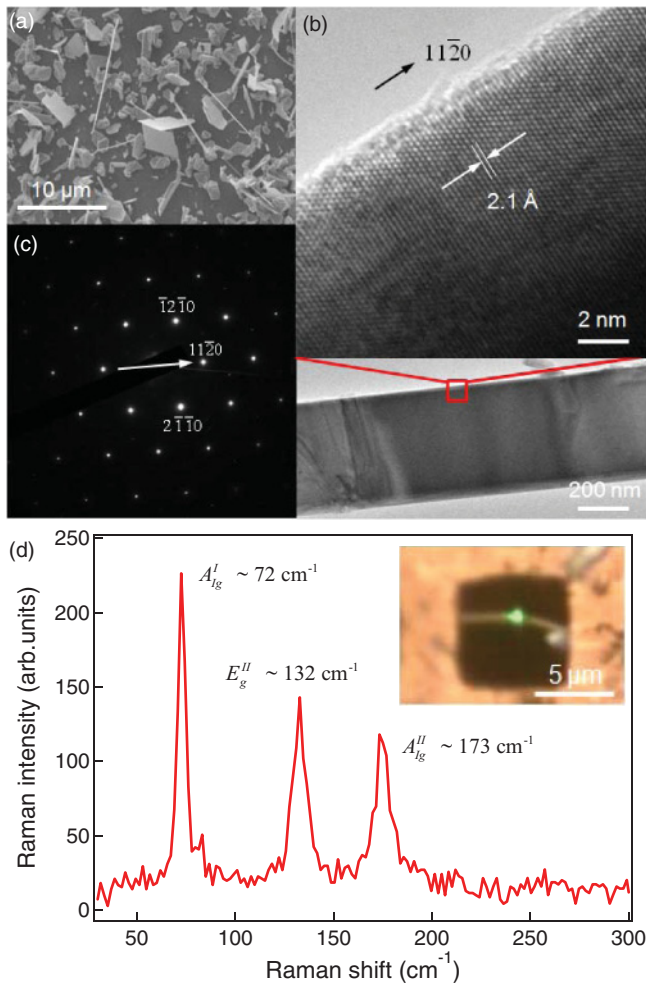
FIG. 1. (Color online) SEM image of as-grown Bi_2Se_3 nanorib-bons on a Si substrate. (b) High-resolution transmission electron microscopy (HRTEM) image from the edge of a Bi_2Se_3 nanoribbon. The interplanar distance along the growth direction [$11\bar{2}0$] is 0.21 nm. (c) Selected area electron diffraction pattern from the nanoribbon in (b) shows hexagonal symmetry. The growth direction is along [$11\bar{2}0$]. (d) A typical Raman spectrum from a single Bi_2Se_3 nanoribbon with 514.5 nm excitation at room temperature. All three vibration modes are consistent with those from bulk Bi_2Se_3. The inset shows an optical image of a nanoribbon supported over a hole of a TEM grid. The spot on the nanoribbon is the laser illumination.

We obtained additional confirmation about the crystalline phase of the samples using Raman spectroscopy of individual Bi_2Se_3 nanoribbons. Figure 1(d) shows a typical room-temperature Raman spectrum from a single Bi_2Se_3 nanoribbon supported over one of the holes in a TEM grid; the data were taken with 514.5 nm excitation and the geometry ensures that the backscattered light only originates from the nanoribbon of interest. The incident radiation was polarized parallel to the nanoribbon growth direction, and the scattered radiation was unpolarized. The measurements were performed with a very low incident laser power ($\sim$10 μW with a spot size of $\sim$ 1 μm) to avoid sample overheating. Three characteristic Raman modes are observed: $\sim$72 cm^{-1}, out-of-plane vibration mode; $\sim$132 cm^{-1}, in-plane vibration mode; and $\sim$173 cm^{-1},
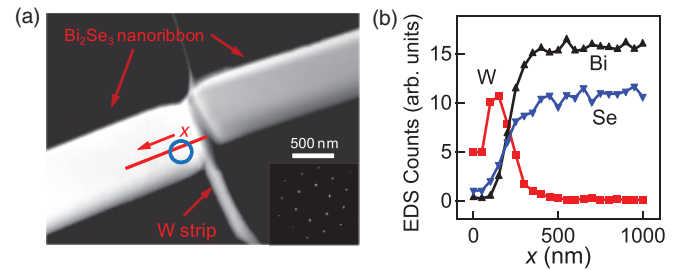

FIG. 2. (Color online) (a) High-angle annular dark field image of a W strip deposited on a Bi_2Se_3 nanoribbon supported on a holey carbon TEM grid using the same deposition conditions for the actual devices. In the region next to the W contact (indicated by the circle), selected area diffraction pattern (inset) shows clear hexagonal Bi_2Se_3 single-crystal structure. The line on the nanoribbon indicates the position of the X-ray energy dispersive spectroscopy (EDS) line profile and the arrow shows the line-scan direction. EDS spectra separated by 50 nm were collected in STEM mode using drift correction. (b) EDS counts (arb. units) vs position plot of elemental W, Bi, and Se. The W signal is within the background at $\sim$450 nm, which corresponds to a spread of $\sim$250 nm from the left visible edge of the tungsten contact.

out-of-plane vibration mode. All these modes are consistent with those observed from bulk Bi_2Se_3.[18]

We fabricated electrical transport devices by transferring as-grown Bi_2Se_3 nanoribbons to a Si substrate with a 1-μm-thick Si_3N_4 insulating layer and then depositing superconducting tungsten and/or normal platinum (Pt) electrodes using a dual beam focused ion beam (FIB) etching and deposition system. The tungsten contacts are contaminated with carbon and gal-lium and, consequently, have a high superconducting transition temperature (4 K $\lesssim T_C \lesssim$ 5 K) and a large critical field ($H_c \gtrsim$ 70 kOe).[19] The correspondingly large superconducting energy gap ($\Delta \sim$ 0.7 meV) allows good energy resolution in differential conductance measurements. Furthermore, the large critical field lends such devices to explorations of possible vortex formation in regions of proximity-induced superconductivity. The FIB method also has the advantage of forming good Ohmic contacts with Bi_2Se_3 nanoribbons, albeit at the price of localized damage in the contact area. TEM measurements of test structures [Fig. 2(a)] show that the nanoribbons remain in the single-crystal Bi_2Se_3 phase after FIB deposition, apart from the region immediately underneath the tungsten contacts. The typical electrode is about 200–400 nm wide and $\sim$50 nm high. X-ray energy dispersive profile scans in scanning TEM studies [Fig. 2(b)] show that the tungsten spreads about 250 nm from the visible edge of the contact. We conservatively estimate that the contacts have a resistance-area product $RA \sim 10^{-10} \Omega m^2$. To rule out the possible shorting between closely spaced tungsten contacts, we also carried out a control measurement by depositing two tungsten strips with a visible edge-to-edge separation of 460 nm on a Si_3N_4 substrate; we found that the (two-probe) resistance of this configuration was larger than 0.5 MΩ at $T = 500$ mK, well below the superconducting transition temperature of the tungsten contacts. To further rule out insidious spreading effects that could occur in a nanostructure geometry, we also examined (undoped) ZnSe nanowires with tungsten contacts and again found no signs of

TABLE I. Summary of Bi_2Se_3 nanoribbon devices.

Device	Length (μm)	Width (nm)	Thickness (nm)	Contact width (nm)	Resistivity at 6 K (mΩ cm)	Contact material
A	1.08	600	60	200	0.51	W
$B1$	0.94	430	60	430	1.37	W
$B2$	1.55	430	60	430	1.37	W
C	2.47	284	276	316	0.79	W
D	2.30	240	77	240	0.70	W
E	5.12	300	98	122	0.69	W
F	1.00	700	60	300	3.53	W
G	5.73	270	60	234	0.39	Pt
H	0.94	370	50	280	0.48	Pt

superconducting shorts below the transition temperature of the contacts.

We measured a total of 6 Bi_2Se_3 nanoribbon devices with tungsten contacts; their characteristics are summarized in Table I. In addition, we also measured two devices with nonsuperconducting (Pt) contacts. Although the nanoribbons were all fabricated in the same synthesis run, their dimensions and electrical properties (resistivity) show an inhomogeneous distribution. We are unable to determine the carrier density and carrier mobility because the nanoribbons are too narrow to carry out Hall effect measurements; however, the electrical resistivity of all the devices ($\sim$1 mΩ cm) is of the same order as typical values observed in thin films of Bi_2Se_3, suggesting similar carrier densities ($n \sim 10^{19}$cm^{-3}). We measured the bias-dependent differential conductance in single Bi_2Se_3 nanoribbon devices using a dc current source and a lock-in amplifier at a frequency of 97 Hz over a temperature range 0.5 K $\leqslant T \leqslant$ 6 K and in magnetic fields up to 80 kOe. The measurements were performed in both four- and two-probe geometries; the latter measurements are carried out in a "pseudo-four-probe" scheme, with two wires on each contact pad.

III. TRANSPORT MEASUREMENTS WITH NORMAL METAL (PT) CONTACTS

Before we discuss transport measurements of Bi_2Se_3 nanoribbons with superconducting electrodes, we first study transport properties of two devices with nonsuperconducting electrodes in the four-probe geometry. Figures 3(a) and 3(b) plot the temperature-dependent conductivity for devices G and H, respectively, showing a $\ln(T)$ variation, consistent with two-dimensional (2D) quantum corrections due to weak antilocalization and electron-electron interactions.[20] Detailed fitting of σ versus T becomes more complicated because of the many fitting parameters: as we show below, fitting the magnetoconductivity to the weak localization theory suggests that there are multiple channels participating in the quantum corrections. Since the slope of σ versus $\ln(T)$ is strongly affected by the dependence of $L_\phi(T)$, it is not appropriate to assume all channels contribute equally, as this assumes the coherence length for each of the channels is the same as the others. Figures 3(c) and 3(d) show the magnetoconductivity for devices G and H at $T = 3.0$ K (squares) and $T = 2.0$ K (circles) in

fields perpendicular to the nanoribbon plane. We fit the magnetoconductivity using the Hikami-Larkin-Nagaoka[21] equation

$$\Delta\sigma_{WL}(H) - \Delta\sigma_{WL}(0) = \alpha \frac{e^2}{2\pi^2\hbar}\left[\Psi\left(\frac{1}{2} + \frac{\hbar c}{4eL_\phi^2 H}\right) - \ln\left(\frac{\hbar c}{4eL_\phi^2 H}\right)\right],$$ (1)

where α depends on the dominant scattering mechanism and $\Psi(x)$ is the digamma function. $\alpha = 1$ in the limit of weak spin orbit and magnetic scattering; $\alpha = -1/2$ in the limit of strong spin-orbit scattering and weak magnetic scattering; and $\alpha = 0$ when magnetic scattering is strong. For completeness, we also include the 2D correction from electron-electron
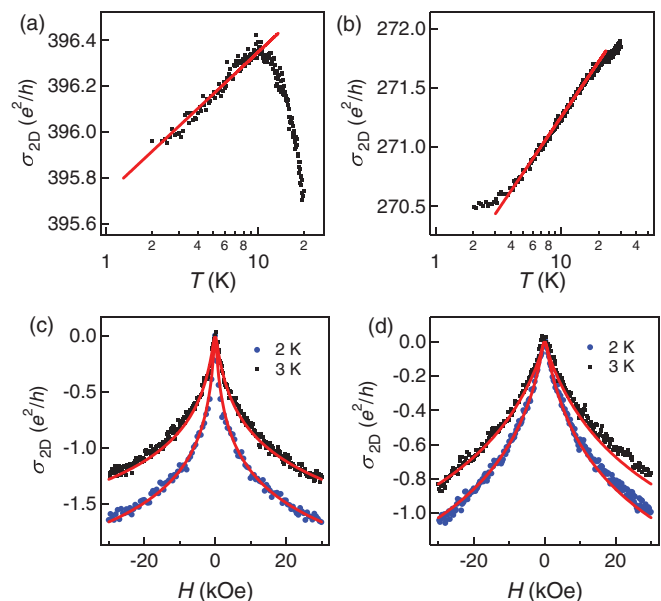

FIG. 3. (Color online) (a) Temperature-dependent conductivity for device G. The solid line is a $\ln(T)$ fit. (b) Temperature-dependent conductivity for device H. The solid line is a $\ln(T)$ fit. (c) Magnetoconductivity for device G at $T = 3.0$ K (squares) and $T = 2.0$ K (circles). The solid lines are fits to the Hikami-Larkin-Nagaoka theory with electron-electron interaction included. (d) Magnetoconductivity for device H at $T = 3.0$ K (squares) and $T = 2.0$ K (circles). The solid lines are fits to the Hikami-Larkin-Nagaoka theory with electron-electron interaction.

interactions[22] given by

$$\Delta\sigma_{\mathrm{EEI}}(T,H) - \Delta\sigma_{\mathrm{EEI}}(T,0) = -\frac{e^2}{4\pi^2\hbar}\tilde{F}_\sigma g_2(T,H), \quad (2)$$

where

$$g_2(T,H) = \int_0^\infty d\Omega \, \ln\left|1 - \left(\frac{g\mu_B H/k_B T}{\Omega}\right)^2\right| \frac{d^2}{d\Omega^2}\frac{\Omega}{e^\Omega - 1}, \quad (3)$$

and $\tilde{F}_\sigma$ is a function of the average of the static screened Coulomb interaction over the Fermi surface. The solid lines in Figs. 3(c) and 3(d) are fits to the above equations, using as fitting parameters the phase-breaking length L_ϕ, the parameter α, and the screening parameter $\tilde{F}_\sigma$. For device G, the fits yield $L_\phi \sim 90.77$ nm, $\alpha = -1.30$, and $\tilde{F}_\sigma = 0.0$ at $T = 3.0$ K and $L_\phi \sim 137.2$ nm, $\alpha = -1.34$, and $\tilde{F}_\sigma = 0.0$ at $T = 2.0$ K. For device H, the fits yield $L_\phi \sim 35.5$ nm, $\alpha = -1.36$, and $\tilde{F}_\sigma = 0.32$ at $T = 3.0$ K and $L_\phi \sim 47.0$ nm, $\alpha = -1.29$, and $\tilde{F}_\sigma = 0.36$ at $T = 2.0$ K. The fitted values of $\alpha \sim -1.3$ implies there is more than one parallel conducting channel contributing to the conductivity.[23] Note that the values of the phase-breaking length are somewhat smaller than typically seen in thin-film samples of Bi_2Se_3.[20]

IV. TRANSPORT MEASUREMENTS WITH SUPERCONDUCTING (TUNGSTEN) CONTACTS: OBSERVATION OF A SUPERCURRENT AND MULTIPLE ANDREEV REFLECTIONS

Figure 4(a) shows the temperature dependence of the two-probe zero-bias differential resistance (dV/dI) of device A with width $w = 600$ nm and thickness $t \sim 60$ nm. The resistance is measured between contacts with edge-to-edge separation $L = 1.08$ μm (SEM image in the inset). Spreading of the tungsten contacts implies a conservatively estimated Bi_2Se_3 channel length of ~ 580 nm. The figure shows the onset of the proximity effect at $T \sim 4.7$ K when the W contacts become superconducting, eventually transitioning to a zero-resistance supercurrent state at $T \leqslant 2$ K. Figure 4(b) plots the I-V characteristics of this device at different temperatures, showing a critical current $I_c = 1.1$ μA at $T = 500$ mK. The product $I_c R_N$ (where R_N is the normal-state resistance) has a small value (~ 165 μV $\ll \frac{\Delta}{e}$), similar to observations in exfoliated Bi_2Se_3 layers.[12] As expected, I_c decreases with increasing temperature until the supercurrent is completely suppressed at $T \geqslant 2$ K.

Figure 4(c) plots dI/dV versus V at $T = 500$ mK, revealing "subharmonic gap structure" due to multiple Andreev
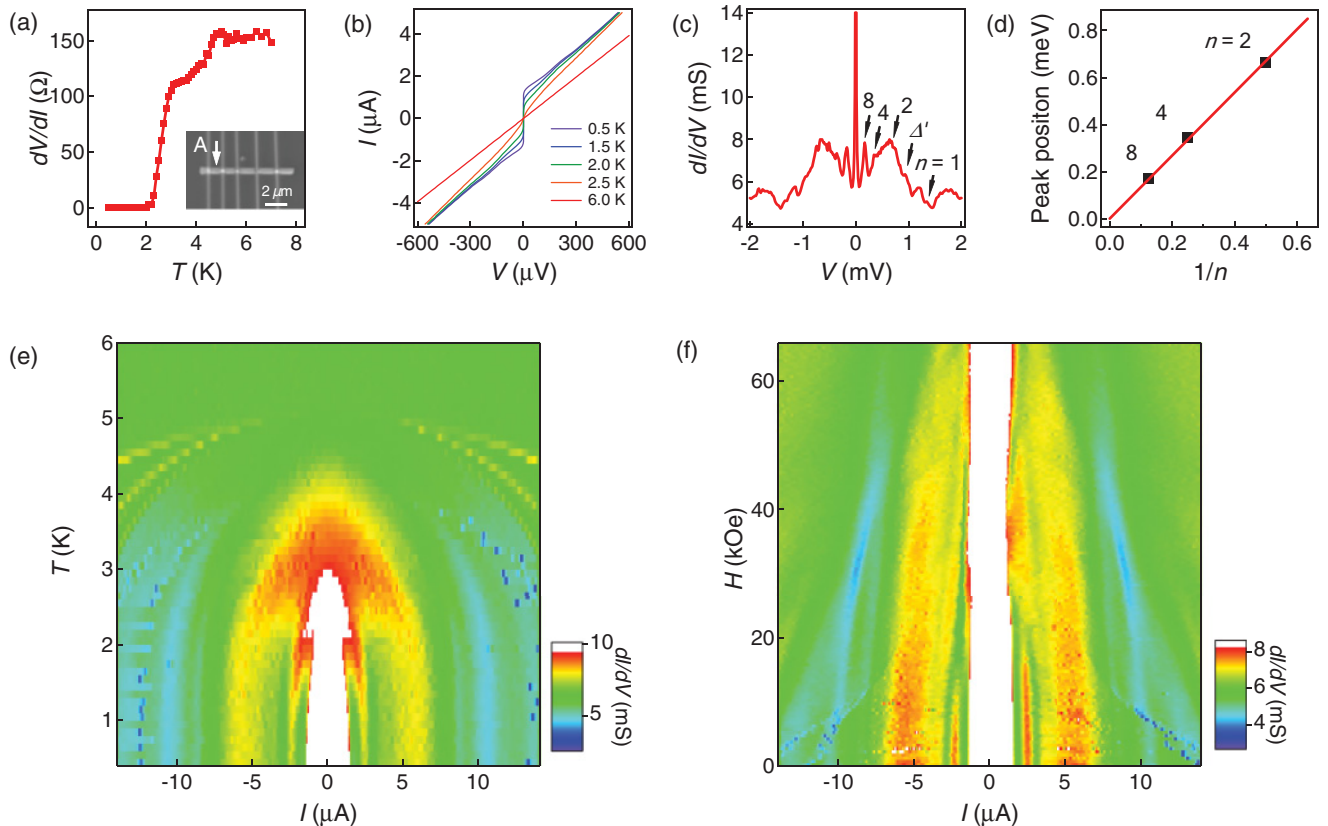

FIG. 4. (Color online) (a) Two-probe zero-bias dV/dI vs temperature for device A at $H = 0$. Inset shows an SEM image of the device, with the arrow indicating the measured channel with edge-to-edge length of 1.08 μm between two W electrodes. (b) I-V characteristics of device A at various temperatures, measured using the same contacts as in (a). (c) dI/dV vs V in device A at $T = 500$ mK and in zero magnetic field. The arrows identify a consistent subharmonic series of conductance anomalies corresponding to subharmonic gap structure ($\frac{2\Delta}{ne}$ with $n = 2,4,8$). (d) Position of differential conductance anomalies as a function of the index $1/n$. (e) Surface plot of dI/dV as a function of the current I and temperature at $H = 0$. (f) Surface plot of dI/dV as a function of the current I and perpendicular magnetic field H at $T = 500$ mK.

reflections at $V = \frac{2\Delta}{ne}$, where Δ is the gap of the W electrodes and n is an integer.[24–27] The arrows identify a consistent series of subharmonic peaks in dI/dV corresponding to $n = 2,4,8$ [Fig. 4(d)] for a superconducting energy gap $\Delta = 0.669$ meV. Using the BCS relation $\Delta = 1.76 k_B T_C$, this corresponds to $T_C = 4.41$ K, which is close to $T_C = 4.7$ K obtained from the temperature-dependent zero-bias differential resistance. The absence of some values of n is not understood, but is not an uncommon occurrence.[26] The peak assignment in Fig. 4(c) results in an anomalous location of the prominent $n = 1$ peak at 1.194 meV instead of the expected location $V = \frac{\Delta}{e} = 1.338$ meV [indicated by the arrow in Fig. 4(c)]. We attribute this to heating at higher bias, noting that similar anomalies have been seen in other SNS devices.[26] The origin of the peak identified as $\Delta' = 0.932$ meV is unclear; it could be a signature of a quasiparticle minigap Δ_g that is expected to arise when $L \sim \sqrt{\hbar D/\Delta} < L_\phi$ (i.e., when the Thouless energy roughly equals the superconducting gap of the S contacts).[25] The data in Figs. 4(a)–4(d) provide a clear indication of proximity-induced superconductivity in Bi$_2$Se$_3$. In Figs. 4(e) and 4(f), we map out the detailed variation of dI/dV as a function of temperature and magnetic field, respectively. These plots show that, as expected from the temperature and field dependence of the superconducting gap of the tungsten electrodes, the multiple Andreev reflection features and I_c are quenched with increasing temperature and field.

Observation of a supercurrent and multiple Andreev reflections in an SNS device requires a normal channel length L shorter than two principal length scales: the thermal length ξ_N, which characterizes the spatial decay of the pair amplitude in the N channel and the electron phase-breaking length L_ϕ. At low temperatures, the cutoff is typically determined by L_ϕ. For diffusive channels ($L > l_{el}$), $\xi_N = \sqrt{\hbar D/2\pi k_B T}$, while for ballistic channels ($L < l_{el}$), $\xi_N = \hbar v_F/2\pi k_B T$. Here, D is the diffusion constant, v_F is the Fermi velocity, k_B is the Boltzmann constant, and T is temperature. Since we do not directly know the carrier density n in our samples, we estimate l_{el} and ξ_N based upon some reasonable assumptions. In the normal state, the magnitudes of the resistivity and magnetoresistance of this nanoribbon (~ 0.51 mΩ cm) are similar to measurements in Bi$_2$Se$_3$ thin films[28] with a carrier density $n \sim 10^{19}$cm^3. We thus use this carrier density as an upper limit for n and use the Drude model ($l_{el} = v_F m_{eff}/\rho n e^2$) to yield $l_{el} \sim 50$ nm, i.e., transport in the channel must be diffusive. By using the experimentally reported effective mass for Bi$_2$Se$_3$, $m_{eff} \approx 0.18 m_e$, at roughly this carrier density and for transport normal to the c axis,[29] we estimate a Fermi velocity $v_F \sim 4 \times 10^5$ms^{-1} from $v_F = \frac{\hbar}{m_{eff}}(3\pi^2 n)^{1/3}$ and a bulk diffusion constant $D \sim 7 \times 10^{-3}$ m^2 s^{-1} from $D = v_F l_{el}/3$. This yields $\xi_N \sim 70$ nm at $T = 1.8$ K. We note that, even if the assumed nanoribbon carrier concentration were an order of magnitude lower (i.e., 10^{18}cm^{-3}), the corresponding mean-free path l_{el} would be ~ 250 nm and thermal length $\xi_N \sim 100$ nm at 1.8 K, both of which are still smaller than the channel length. Next, we estimate a lower bound for L_ϕ by extracting the electron inelastic length from weak antilocalization fits to the magnetoconductance of Bi$_2$Se$_3$ nanoribbons with normal metal (Pt) contacts. (The large H_c for the W contacts precludes a direct measurement of

the low-temperature magnetoconductance in samples with superconducting contacts.) In the two devices measured [Figs. 3(c) and 3(d)], we find $L_\phi \lesssim 140$ nm at $T = 2$ K.

Thus, our analysis shows that we are observing a supercurrent and multiple Andreev reflections in SNS junctions with N channel lengths that are significantly longer than the values for ξ_N and L_ϕ deduced from the diffusive normal-state transport. The simplest explanation for this apparent inconsistency is the coexistence of ballistic (surface) and diffusive (bulk) transport channels. We speculate that the latter may dominate the transport in the normal state, but that the proximity-induced superconductivity preferentially occurs in the ballistic surface channel. The validity of this conjecture can be checked by estimating ξ_N in the ballistic limit, using the value of the Fermi velocity $v_F \sim 5 \times 10^5$ms^{-1} for the TI surface state in Bi$_2$Se$_3$;[30] this yields a value $\xi_{N(clean)} = \frac{\hbar v_F}{2\pi k_B T} \sim 340$ nm at $T = 1.8$ K, which is more consistent with the observation of a supercurrent at comparable channel lengths.

Our hypothesis of a ballistic surface channel that preferentially supports proximity-induced superconductivity is bolstered by transport measurements in three other Bi$_2$Se$_3$ nanoribbon devices. Figure 5 presents data taken on device
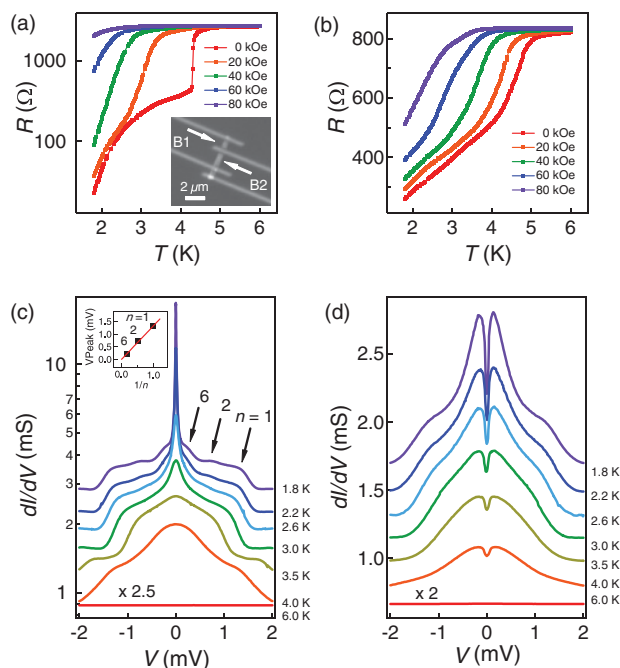

FIG. 5. (Color online) (a) Two-probe resistance vs temperature for channel $B1$ in different perpendicular fields. Inset shows an SEM image of the device B, with the two arrows indicating channels $B1$ and $B2$ with edge-to-edge length of 0.94 and 1.55 μm, respectively, between two W electrodes. (b) Four-probe resistance vs temperature for channel $B2$ in different perpendicular fields. (c) dI/dV vs V for channel $B1$ at different temperatures and in zero magnetic field using a two-probe configuration. Data for different temperatures are shifted or scaled with respect to the curve at $T = 4.0$ K for clarity. The arrows indicate conductance peaks corresponding to subharmonic gap structure ($2\Delta/ne$ with $n = 1,2,6$). (d) dI/dV vs V for channel $B2$ at different temperatures and in zero magnetic field using a two-probe configuration. The data for different temperatures are shifted or scaled with respected to the curve at $T = 4.0$ K for clarity.

B, a Bi$_2$Se$_3$ nanoribbon of thickness $t = 60$ nm and width $w = 430$ nm. The normal-state resistivity of this nanoribbon (1.37 mΩ cm) is almost three times greater than device *A*, yielding shorter estimated elastic and thermal lengths ($l_{el} \sim 20$ nm, $\xi_N \sim 40$ nm). This device has two measurable channels [*B*1 and *B*2 in the inset to Fig. 5(a)] with conservatively estimated channel lengths $L_{B1} \sim 0.44 \mu$m and $L_{B2} \sim 1.05 \mu$m, respectively. Figures 5(a) and 5(b) show the onset of the proximity effect in these channels, while Figs. 5(c) and 5(d) show the bias-dependent differential conductance. The presence of multiple Andreev reflections in channel *B*1 and their absence in channel *B*2 are both consistent with our earlier estimate of $\xi_{N(clean)} \sim 340$ nm for a clean surface channel since $L_{B1} \sim \xi_{N(clean)} \ll L_{B2}$. We have also observed subharmonic gap structure in two additional nanoribbons (not shown). The overall behavior is similar to that discussed above.

V. TRANSPORT MEASUREMENTS WITH SUPERCONDUCTING (TUNGSTEN) CONTACTS: ANOMALOUS MAGNETORESISTANCE OSCILLATIONS

We now discuss the occurrence of unusual MR oscillations in Bi$_2$Se$_3$ nanoribbons under conditions where the

contacts become superconducting, but where a supercurrent has not yet been established. In order to make consistent comparisons, we carried out both sets of measurements in the two-probe geometry on device *B*, recalling that the electrode configuration shown in Fig. 5(a) precludes a true four-probe measurement for the shorter channel. As a check, we also measured channel *B*2 in the four-probe geometry and found identical behavior as in the two-probe measurements. Figure 6(a) shows the MR for channel *B*1 at $T = 2.2$ K with a magnetic field applied perpendicular to the plane of the nanoribbon. At low field ($|H| < 0.6$ kOe), we observe a sharp cusp characteristic of weak antilocalization, similar to earlier results from Bi$_2$Se$_3$ nanoribbons contacted with normal electrodes. However, at higher fields, we find well-defined and reproducible MR oscillations superimposed on a smooth background. The inset to Fig. 6(a) plots the magnetic field position of both peaks and valleys. If we exclude the low-field region, we find that the MR oscillations are periodic in H with a period $\Delta H \sim 3.22$ kOe. Figure 6(b) shows that the oscillation amplitude varies nonmonotonically with temperature, reaching a maximum in the vicinity of $T = 2.2$ K and vanishing at both lower and higher temperatures. Similar behavior is observed in channel *B*2 except with a
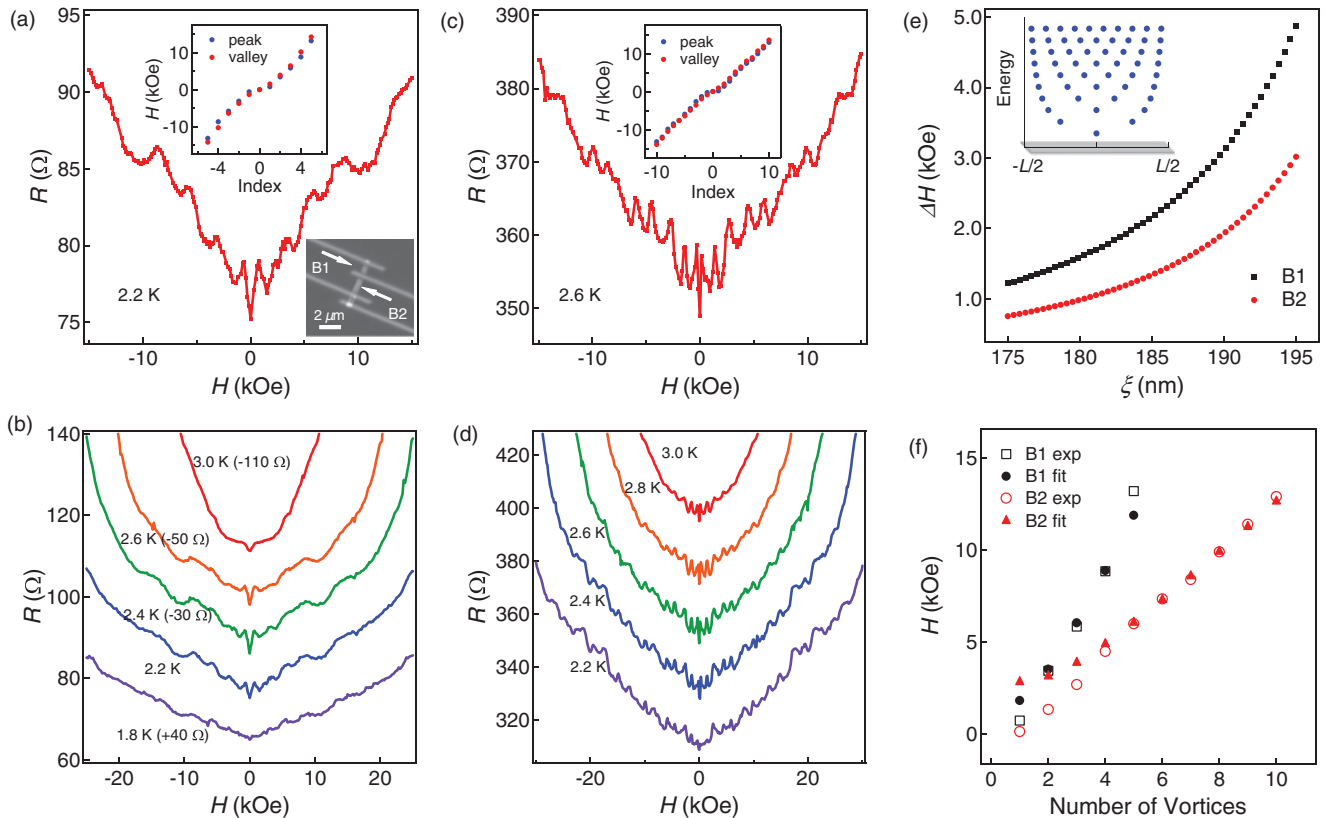

FIG. 6. (Color online) (a) MR in device *B* (channel *B*1, see lower inset) at $T = 2.2$ K. The upper inset plots the position of both peaks and valleys. (b) MR in channel *B*1 at different temperatures. The data are shifted with respect to the data at $T = 2.2$ K for clarity. (c) MR in channel *B*2 at $T = 2.6$ K. The inset plots the position of both peaks and valleys. (d) MR in channel *B*2 at different temperatures. The magnetic field in panels (a)–(d) is perpendicular to the nanoribbon plane. (e) Calculated MR oscillation period vs coherence length (size of vortex) for channels *B*1 (squares) and *B*2 (circles). Comparison with the data in Figs. 2(a) and 2(c) yields $\xi = 191$ and 186 nm for channels *B*1 and *B*2, respectively. The inset is a model calculation showing how vortices distribute in a nanoribbon as the energy (magnetic field) increases. (f) Magnetic field vs number of vortices. Open symbols are experimental data and filled symbols are fits using the values of ξ obtained in panel (e).
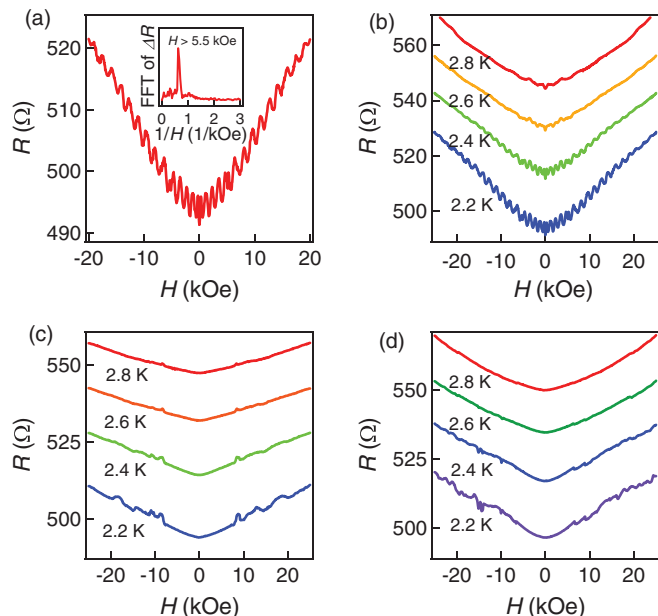
FIG. 7. (Color online) (a) MR for device D at $T = 2.2$ K in field perpendicular to nanoribbon plane using four-probe geometry. Pronounced and reproducible MR oscillations with a period of $\Delta H \sim 1.6$ kOe for $|H| > 5.5$ kOe were observed. The inset is the fast Fourier transform (FFT) of the MR after a smooth background is subtracted for $H > 5.5$ kOe. (b) MR at different temperatures for device D in field perpendicular to the plane of the nanoribbon. (c) MR at different temperatures for device D in field parallel to the axis of the nanoribbon. (d) MR at different temperatures for device D in field parallel to the plane but perpendicular to the axis of the nanoribbon.

smaller period $\Delta H \sim 1.44$ kOe [Figs. 6(c) and 6(d)]. Similar oscillatory MR has also been observed in two other devices. For example, Fig. 7 shows the MR of device D in three primary field orientations: perpendicular to the plane of the nanoribbon [Figs. 7(a) and 7(b)], parallel to the nanoribbon axis [Fig. 7(c)], and parallel to the plane but perpendicular to the axis of the nanoribbon [Fig. 7(d)]. While similar MR oscillations that are periodic ($\Delta H \sim 1.60$ kOe) at higher field were observed when the field is perpendicular to the nanoribbon plane, they were not observed in the other two primary field directions.

The observed MR oscillations can not be explained using standard scenarios. The Shubnikov–de Haas effect is ruled out since the oscillations are not periodic in $1/H$. The Aharonov-Bohm effect of surface currents[16] is also ruled out for several reasons: the oscillations are only observed when the magnetic field is perpendicular to the nanoribbon plane and not when it is parallel; the oscillation amplitude has a nonmonotonic temperature dependence; finally, MR oscillations are absent when using normal metal contacts (e.g., Pt down to $T = 2$ K or W contacts above the superconducting transition temperature), clearly indicating the important role of superconductivity. We note that the Aharonov-Bohm oscillations were not observed in device D in parallel field due to the dominance of the normal transport in a long channel ($L \gg \xi_{N(clean)}$) even when the electrodes are in the superconducting state.

We also discount another conventional explanation for the oscillatory MR, namely, fluxoid quantization, which requires a multiply connected geometry where flux can penetrate normal regions encompassed by a superconductor.[31] Assuming fluxoid quantization, the observed oscillation period implies a characteristic geometrical area $A = (h/2e)(\Delta H)^{-1} = 0.643 \times 10^4 \text{nm}^2$ and 1.44×10^4 nm^2 for channels $B1$ and $B2$, respectively. This is far smaller than any relevant geometrical region in our devices. The scaling of the oscillation period with the length of the Bi_2Se_3 channel ($B1$ and $B2$), roughly doubling when the channel length is halved, further rules out any insidious fluxoid quantization that might be associated with FIB damage in the contact region.

Having dismissed standard explanations for our observations, we resort to a model that predicts MR oscillations when a thin, narrow superconducting strip is placed in a perpendicular magnetic field.[15,32] We are cautiously aware that this "Weber blockade" model was developed for a genuine superconductor, while we are assuming that it can also be applied to a normal metal supporting proximity-induced superconductivity. There is a theoretical basis for the formation of vortexlike pair correlations in the N region of diffusive SNS junctions,[33] but we are unaware of a similar prediction for a ballistic case such as the proximity effect in a high-mobility TI surface state. In the Weber blockade model, the perpendicular magnetic field controls the number of Pearl vortices in the superconducting strip. Maximum dissipation (i.e., maximum resistance) occurs when the energies of configurations with N and $N + 1$ vortices are degenerate, and the MR then has a period related to the sequential addition of vortices with increasing magnetic field. Certain observations are immediately consistent with this model: for instance, the onset of periodic oscillations occurs only after a finite field [see insets to Figs. 6(a) and 6(c)] and the oscillation period is larger than that expected using fluxoid quantization in the geometric area of the channel. Assuming that a proximity-induced superconductor can be described by a uniform superconducting coherence length ξ (distinct from the length scale of the diffusion of Cooper pairs into the superconductor), this model can be extended to predict ξ in the region of proximity-induced superconductivity for our geometry.

Using the geometrical parameters for our nanoribbons, we calculated the period of the MR oscillation as a function of the coherence length ξ (i.e., the size of a vortex). Figure 6(e) shows the result of this calculation for channels $B1$ and $B2$, with channel width of 430 nm and nominal channel lengths of 0.94 μm (squares) and 1.55 μm (circles), respectively. A comparison with the experimentally observed period yields $\xi = 191(186)$ nm for channel $B1$ ($B2$). This length scale corresponds to the size of a vortex in the Bi_2Se_3 channel and, as expected, is much larger than the coherence length of a typical superconductor (such as the tungsten contacts). The inset to Fig. 6(e) shows, in a model calculation, how vortices distribute in a nanoribbon as the energy (magnetic field) increases. In Fig. 6(f), we plot the number of vortices in the channel as a function of the applied magnetic field, assuming the fitted values of ξ in Fig. 6(e). The model assumes a uniform superconducting gap; this may account for the disagreement between the experiment and

the calculation using the fitted value of ξ for the first few vortices [Fig. 6(f)].

VI. CONCLUSIONS

In summary, we have demonstrated proximity-induced superconductivity in Bi_2Se_3 nanoribbons contacted with superconducting electrodes. Our experiments suggest that even when diffusive bulk conduction coexists with ballistic surface conduction in a 3D TI, the proximity effect may preferentially couple to the latter. Furthermore, the superconductor-TI device configuration demonstrated here provides a viable route for creating vortices near the interface between these two classes of materials. The formation of these vortices is manifest in MR oscillations, the period of which can be well explained using a simple model. Thus, our experiments show that superconductivity, and possibly vortices, can be realized in experimental geometries that are directly relevant to the search for Majorana fermions in condensed matter systems.[4–6]

*nsamarth@psu.edu

[1] B. Pannetier and H. Courtois, J. Low Temp. Phys. **118**, 599 (2000).

[2] M. Z. Hasan and C. L. Kane, Rev. Mod. Phys. **82**, 3045 (2010).

[3] X.-L. Qi and S.-C. Zhang, Rev. Mod. Phys. **83**, 1057 (2011).

[4] L. Fu and C. L. Kane, Phys. Rev. Lett. **100**, 096407 (2008).

[5] J. D. Sau, R. M. Lutchyn, S. Tewari, and S. Das Sarma, Phys. Rev. B **82**, 094522 (2010).

[6] A. Cook and M. Franz, e-print arXiv:1105.1787.

[7] T. D. Stanescu, J. D. Sau, R. M. Lutchyn, and S. Das Sarma, Phys. Rev. B **81**, 241310(R) (2010).

[8] J. Wang, C.-Z. Chang, H. Li, K. He, M. Singh, X.-C. Ma, M. Xie, Q.-K. Xue, and M. H. W. Chan, e-print arXiv:1105.6174.

[9] A. Y. Kasumov, O. V. Kononenko, V. N. Matveev, T. B. Borsenko, V. A. Tulin, E. E. Vdovin, and I. I. Khodos, Phys. Rev. Lett. **77**, 3029 (1996).

[10] L. Fu, C. L. Kane, and E. J. Mele, Phys. Rev. Lett. **98**, 106803 (2007).

[11] D. Hsieh, D. Qian, L. Wray, Y. Xia, Y. S. Hor, R. J. Cava, and M. Z. Hasan, Nature (London) **452**, 970 (2008).

[12] B. Sacepe, J. B. Oostinga, J. Li, A. Ubaldini, N. J. G. Couto, E. Giannini, and A. F. Morpurgo, e-print arXiv:1101.2352.

[13] Y. S. Hor, A. J. Williams, J. G. Checkelsky, P. Roushan, J. Seo, Q. Xu, H. W. Zandbergen, A. Yazdani, N. P. Ong, and R. J. Cava, Phys. Rev. Lett. **104**, 057001 (2010).

[14] L. A. Wray, S.-Y. Xu, Y. Xia, Y. S. Hor, D. Qian, A. V. Fedorov, H. Lin, A. Bansil, R. J. Cava, and M. Z. Hasan, Nat. Phys. **6**, 855 (2010).

[15] D. Pekker, G. Refael, and P. M. Goldbart, Phys. Rev. Lett. **107**, 017002 (2011).

[16] H. Peng, K. Lai, D. Kong, S. Meister, Y. Chen, X.-L. Qi, S.-C. Zhang, Z.-X. Shen, and Y. Cui, Nat. Mater. **9**, 225 (2010).

[17] D. S. Kong J. C. Randel, H. Peng, J. J. Cha, S. Meister, K. Lai, Y. Chen, Z.-X. Shen, H. C. Manoharan, and Y. Cui, Nano Lett. **10**, 329 (2010).

[18] W. Richter, H. Kohler, and C. R. Becker, Phys. Status Solidi B **84**, 619 (1977).

[19] J. Wang, M. Singh, M. Tian, N. Kumar, B. Liu, C. Shi, J. K. Jain, N. Samarth, T. E. Mallouk, and M. H. W. Chan, Nat. Phys. **6**, 389 (2010).

[20] J. Wang, A. M. DaSilva, C.-Z. Chang, K. He, J. K. Jain, N. Samarth, X.-C. Ma, Q.-K. Xue, and M. H. W. Chan, Phys. Rev. B **83**, 245438 (2011).

[21] S. Hikami, A. I. Larkin, and Y. Nagaoka, Prog. Theor. Phys. **63**, 707 (1980).

[22] P. A. Lee and T. V. Ramakrishnan, Rev. Mod. Phys. **57**, 287 (1985).

[23] H. Steinberg, J.-B. Laloe, V. Fatemi, J. S. Moodera, and P. Jarillo-Herrero, e-print arXiv:1104.1404.

[24] M. Octavio, M. Tinkham, G. E. Blonder, and T. M. Klapwijk, Phys. Rev. B **27**, 6739 (1983).

[25] J. C. Cuevas, J. Hammer, J. Kopu, J. K. Viljas, and M. Eschrig, Phys. Rev. B **73**, 184505 (2006).

[26] J. Xiang, A. Vidan, M. Tinkham, R. M. Westervelt, and C. M. Lieber, Nat. Nanotechnol. **1**, 208 (2006).

[27] H. B. Heersche, P. Jarillo-Herrero, J. B. Oostinga, L. M. K. Vandersypen, and A. F. Morpurgo, Nature (London) **446**, 56 (2007).

[28] A. Richardella, D. M. Zhang, J. S. Lee, A. Koser, D. W. Rench, A. L. Yeats, B. B. Buckley, D. D. Awschalom, and N. Samarth, Appl. Phys. Lett. **97**, 262104 (2010).

[29] G. R. Hyde, H. A. Beale, I. L. Spain, and J. A. Woollam, J. Phys. Chem. Solids **35**, 1719 (1974).

[30] H. J. Zhang, C.-X. Liu, X.-L. Qi, X. Dai, Z. Fang, and S.-C. Zhang, Nat. Phys. **5**, 438 (2009).

[31] I. Sochnikov, A. Shaulov, Y. Yeshurun, G. Logvenov, and I. Bozovic, Nat. Nanotechnol. **5**, 516 (2010).

[32] A. Johansson, G. Sambandamurthy, D. Shahar, N. Jacobson, and R. Tenne, Phys. Rev. Lett. **95**, 116805 (2005).

[33] J. C. Cuevas and F. S. Bergeret, Phys. Rev. Lett. **99**, 217002 (2007).